

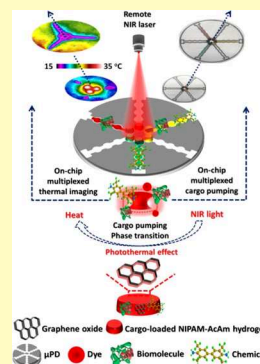
# Spatiotemporally Controlled Multiplexed Photothermal Microfluidic Pumping under Monitoring of On-Chip Thermal Imaging

Guanglei Fu,<sup>\*,†</sup> Yabin Zhu,<sup>†</sup> Weihua Wang,<sup>‡</sup> Mi Zhou,<sup>†</sup> and XiuJun Li<sup>\*,§</sup><sup>†</sup>Biomedical Engineering Research Center, Medical School of Ningbo University, Ningbo 315211, Zhejiang, P. R. China<sup>‡</sup>The Affiliated Hospital of Medical School of Ningbo University, Ningbo 315020, Zhejiang, P. R. China<sup>§</sup>Department of Chemistry and Biochemistry, University of Texas at El Paso, 500 West University Avenue, El Paso, Texas 79968, United States

## Supporting Information

**ABSTRACT:** Intelligent contactless microfluidic pumping strategies have been increasingly desirable for operation of lab-on-a-chip devices. Herein, we present a photothermal microfluidic pumping strategy for on-chip multiplexed cargo transport in a contactless and spatiotemporally controllable fashion based on the application of near-infrared laser-driven photothermal effect in microfluidic paper-based devices ( $\mu$ PDs). Graphene oxide (GO)-doped thermoresponsive poly(*N*-isopropylacrylamide)-acrylamide hydrogels served as the photothermally responsive cargo reservoirs on the  $\mu$ PDs. In response to remote contactless irradiation by an 808 nm laser, on-chip phase transition of the composite hydrogels was actuated in a switchlike manner as a result of the photothermal effect of GO, enabling robust on-chip pumping of cargoes from the hydrogels to predefined arrays of reaction zones. The thermal imaging technique was employed to monitor the on-chip photothermal pumping process. The microfluidic pumping performance can be spatiotemporally controlled in a quantitative way by remotely tuning the laser power, irradiation time, and GO concentration. The pumping strategy was exemplified by  $\text{FeCl}_3$  and horseradish peroxidase as the model cargoes to implement on-chip Prussian blue- and 3,3',5,5'-tetramethylbenzidine-based colorimetric reactions, respectively. Furthermore, multiplexed on-demand microfluidic pumping was achieved by flexibly adjusting the irradiation pathway and the microfluidic pattern. The new microfluidic pumping strategy shows great promise for diverse microfluidic applications due to its flexibility, high integratability into lab-on-a-chip devices, and contactless and spatiotemporal controllability.

**KEYWORDS:** NIR laser-driven photothermal effect, microfluidic pumping, responsive hydrogel, graphene oxide, thermal imaging



## INTRODUCTION

Microfluidic devices have emerged as a promising platform in a wide range of applications because of their unique advantages, such as portability, low-cost, and ease of operation.<sup>1–6</sup> In recent years, various microfluidic devices using different working principles have been developed for diverse microfluidic applications, especially for point-of-care testing.<sup>7–16</sup> It has been well established that the on-chip handling of fluids and cargoes is one of the most crucial steps in microfluidic operations.<sup>17,18</sup> Despite great research progress, these microfluidic devices usually have to be confronted with several challenges in lab-on-a-chip applications.<sup>17,19</sup> In particular, the requirement of external pumping accessories, such as pipettes, fluid storage bottles, and connection tubules, with inevitable physical contact with the devices limits their integratability into lab-on-a-chip devices.<sup>17,19,20</sup> Therefore, there is an increasing demand for the development of new intelligent contactless microfluidic pumping strategies.

Responsive hydrogels have been the subject of extensive research due to their capability to perform “smart” structural changes upon external stimulus.<sup>17,19,21–25</sup> Owing to the intrinsic hydrophilic character of polymerized three-dimen-

sional (3D) hydrogel networks, hydrogels are excellent reservoirs for storage of liquid cargoes.<sup>26–29</sup> Among various responsive hydrogels, thermoresponsive hydrogels are of particular interest because of their reversible and sensitive phase-transition behavior in response to temperature changes.<sup>22,30–32</sup> For instance, the poly(*N*-isopropylacrylamide) (NIPAM)-derived hydrogels exist in swollen states at temperatures below their lower critical solution temperature (LCST) and undergo progressive collapse at temperatures above the LCST with the release of incorporated liquids.<sup>22,30,33,34</sup> The NIPAM-derived hydrogels had been used as cargo reservoirs to implement fluidic protocols on microfluidic devices by an external heating plate as the heat source.<sup>17,19</sup> Although some handheld heating elements can serve as the heat sources,<sup>17</sup> a physical contact between the heating elements and the microfluidic devices is inevitable. In comparison with a switchlike instant controlling manner, the contact-based heating approach compromises the sensitivity and controll-

Received: June 17, 2019

Accepted: August 27, 2019

Published: August 27, 2019

ability toward phase transition of the hydrogels. In addition, the flexibility and targeting capability of the heating approach are challenging, especially in some complex microfluidic arrays with varying heating requirements. In combination with intelligent responsive hydrogels, the introduction of new physical and chemical pumping principles in microfluidic devices offers new opportunities to cope with these limitations.

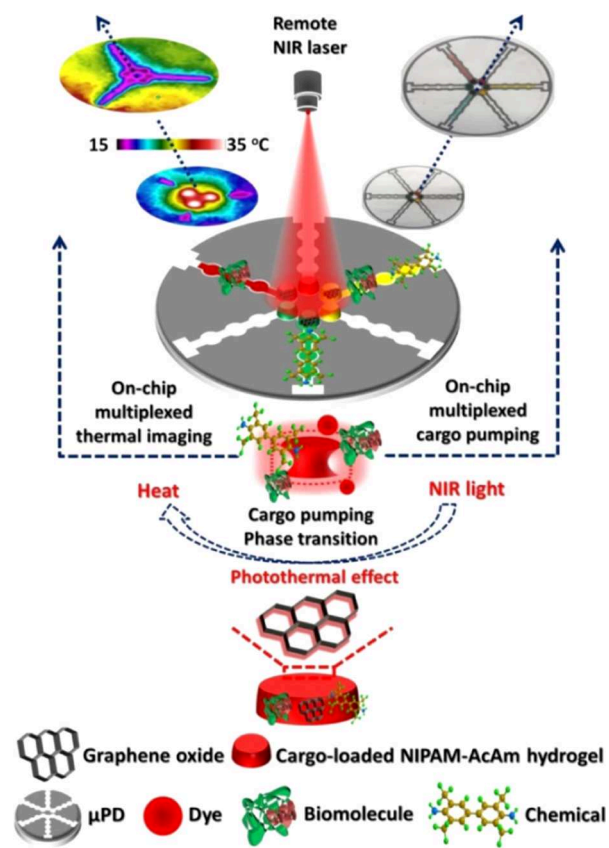
Near-infrared (NIR) laser-driven photothermal effect has attracted increasing research interest, especially for targeted photothermal therapy of cancers.<sup>35–37</sup> A great number of materials with strong photothermal conversion efficiency in the NIR region have been developed as photothermal agents.<sup>38–41</sup> As a unique type of external stimulus, the NIR laser is of particular advantage for lab-on-a-chip operations because of its high integratability into lab-on-a-chip devices and remote targeting capability without any physical contact with the target. More importantly, the NIR laser-driven photothermal effect can be controlled remotely by tuning the parameter settings of the laser pointers in a spatiotemporal fashion.<sup>42,43</sup> Using photothermally responsive hydrogels as the liquid valves, the NIR laser-driven photothermal effect had been adopted to control fluid flow in quartz tubes.<sup>44</sup> Since miniaturized laser arrays with adjustable working parameters are becoming commercially available, the NIR laser-driven photothermal effect holds great potential as a novel pumping principle in microfluidic devices. However, to the best of our knowledge, the NIR laser-driven photothermal effect has rarely been exploited in microfluidic devices, especially for on-chip multiplexed cargo transport.

Based on the application of the NIR laser-driven photothermal effect in microfluidic paper-based devices ( $\mu$ PDs) in combination with photothermally responsive hydrogels, we herein present a photothermal microfluidic pumping strategy for on-chip multiplexed cargo transport under monitoring of on-chip thermal imaging, as shown in Scheme 1. Graphene oxide (GO)-doped NIPAM–acrylamide (NIPAM–AcAm) hydrogels serve as the photothermally responsive cargo reservoirs on the  $\mu$ PDs. In response to remote irradiation by an 808 nm laser, photothermal effect of GO actuates on-chip phase transition of the cargo-loaded hydrogels, enabling highly robust on-chip pumping of cargoes from the hydrogels in a contactless and spatiotemporally controllable fashion. The thermal imaging technique is employed to monitor the on-chip photothermal microfluidic pumping process. Off-chip photothermal responsiveness of the hydrogels as well as their on-chip microfluidic pumping performance is studied systematically. The microfluidic pumping strategy is exemplified by  $\text{FeCl}_3$  and horseradish peroxidase (HRP) as the model cargoes to implement on-chip Prussian blue (PB)- and 3,3',5,5'-tetramethylbenzidine (TMB)-based colorimetric reactions, respectively. Furthermore, multiplexed on-demand microfluidic pumping is achieved by flexibly adjusting the irradiation pathway and the microfluidic pattern. The new microfluidic pumping strategy is particularly promising to meet the requirements of diverse microfluidic liquid- and cargo-handling protocols because of its flexibility, high integratability into lab-on-a-chip devices, and contactless and spatiotemporal controllability.

## EXPERIMENTAL SECTION

**Materials and Instruments.** Whatman chromatography papers (grade no. 1) were purchased from GE Healthcare Worldwide (Shanghai, China). Laser irradiation was performed by employing an

**Scheme 1. Schematic Illustration of Principle of the Photothermal Microfluidic Pumping Strategy**



808 nm diode laser (MDL-III-808) equipped with a power adjustor (Changchun New Industries Optoelectronics Technology Co., Ltd., Changchun, China). Photographs and thermal images of  $\mu$ PDs were taken with a Canon EOS 600D camera (Canon Inc., Tokyo, Japan) and a FLIR C2 thermal camera (FLIR Systems Inc., CA), respectively (see the Supporting Information).

**Procedures for On-Chip Photothermal Microfluidic Pumping.** Microfluidic patterns were printed on chromatography papers by employing a wax printer (Xerox Phaser 8560, Fuji Xerox Co., Ltd., Japan) (see the Supporting Information). The hydrogel rods (6.0 mm in diameter, see the synthesis procedure in the Supporting Information) were uniformly sliced into circular pieces of 2.0 mm thickness. The hydrogel pieces were thoroughly dried on filter papers and then loaded on reservoirs of the  $\mu$ PDs. To actuate phase transition of the hydrogels and the simultaneous on-chip pumping of cargoes, the hydrogel pieces were exposed to an 808 nm laser at different powers for different times. Thermal images of the  $\mu$ PDs were taken and quantitatively analyzed with FLIR Tools software. Photographs of the  $\mu$ PDs were taken after 15 min upon removal of laser irradiation. It should be noted that all experiments were carried out at an atmosphere with a room temperature of around 11.0 °C, except the experiment shown in Figure 3A,B (i.e., 18.0 °C).

**Procedures for Exemplification of the Photothermal Microfluidic Pumping Strategy.**  $\text{FeCl}_3$  and HRP were chosen as the model cargoes to implement the PB- and TMB-based colorimetric reactions, respectively, on the 3D foldable  $\mu$ PD. Potassium ferrocyanide solution (4.0  $\mu\text{L}$ , 10 mM) and 3.0  $\mu\text{L}$  of TMB– $\text{H}_2\text{O}_2$  substrate solution were pipetted into each reaction well on the  $\mu$ PD to act as the substrates of the PB- and TMB-based colorimetric reactions, respectively. After drying the  $\mu$ PD at room temperature for 1.0 h, the reaction zone was folded toward the pumping zone to enable the compact contact between the reaction wells and the pumping channels. The hydrogel pieces (4.0 mm in thickness) loaded with different concentrations of  $\text{FeCl}_3$  and HRP solutions were

irradiated on the reservoirs by the 808 nm laser for 130 s at a power density of  $2.2 \text{ W}\cdot\text{cm}^{-2}$ . After 15 min upon the removal of the laser irradiation, photographs of the  $\mu\text{PDs}$  were taken and analyzed with ImageJ software.

**Procedures for Multiplexed Photothermal Microfluidic Pumping.** To implement multiplexed photothermal microfluidic pumping on the disklike  $\mu\text{PD}$ , the spatial distance between the  $\mu\text{PD}$  and the laser pointer was adjusted to 11.5 cm to obtain a light spot of 2.6 cm in diameter on the  $\mu\text{PD}$ . Six pieces of the hydrogels loaded with different dye solutions were simultaneously irradiated on the central reservoirs by a single irradiation process for 150 s at a power density of  $0.38 \text{ W}\cdot\text{cm}^{-2}$ . After irradiation, thermal images of the  $\mu\text{PDs}$  were taken immediately.

## RESULTS AND DISCUSSION

**Synthesis and Characterization of Hydrogels.** The thermoresponsive hydrogels were synthesized via the typical radical polymerization method using NIPAM and AcAm as the monomers.<sup>17</sup> It had been reported that the NIPAM–AcAm hydrogel showed a broader temperature-responsive range over the pure NIPAM hydrogel, owing to the enhanced hydrogen-bonding capability of the polymer chains after copolymerization with AcAm.<sup>17</sup> To synthesize GO-doped composite hydrogels, GO dispersions were doped in the monomer solutions before the initiation of the polymerization reaction. The as-obtained composite hydrogel showed a transparent brown color due to the doping of GO, as shown in Figure 1C.

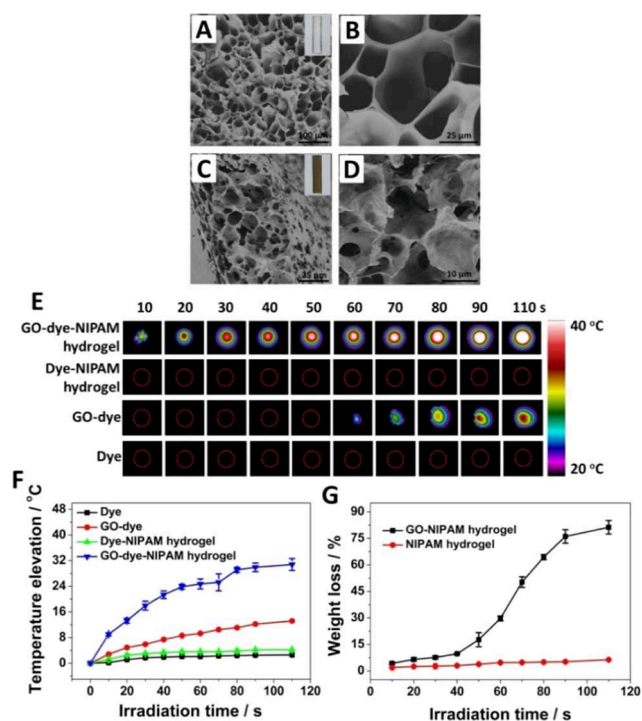


**Figure 1.** Characterization and off-chip photothermal responsiveness of hydrogels. SEM images of the blank NIPAM–AcAm hydrogel at (A) low and (B) high magnification, and of the GO-doped NIPAM–AcAm composite hydrogel at (C) low and (D) high magnification. (E) Thermal images of the hydrogels, dye solutions ( $64 \mu\text{L}$ ), and GO dispersions ( $0.5 \text{ mg mL}^{-1}$ ,  $64 \mu\text{L}$ ) after laser irradiation for different times at a power density of  $2.2 \text{ W}\cdot\text{cm}^{-2}$ . (F) Temperature elevations of the samples at various irradiation times. (G) Weight loss of the hydrogels as a function of irradiation time. Inset: Photographs of the hydrogels. Laser irradiation of aqueous samples was carried out in a 96-well plate. Error bars indicate standard deviations ( $n = 3$ ).

As can be seen from the scanning electron microscopy images of the freeze-dried hydrogels, both the blank NIPAM–AcAm hydrogel (Figure 1A,B) and the GO-doped composite hydrogel (Figure 1C,D) exhibited the characteristic 3D macroporous structures of hydrogels. Large amounts of liquid solutions can be incorporated into these 3D networks during the swelling processes of the hydrogels.<sup>17,22,30</sup> The blank NIPAM–AcAm hydrogel showed a smooth polymer matrix, whereas the composite hydrogel displayed relatively rougher networks with smaller pore sizes. GO nanosheets were observed to be uniformly distributed in the hydrogel matrix with obvious attachment on the polymer walls.

Herein, GO as the NIR laser-driven photothermal nanomaterial<sup>45–47</sup> was proposed to trigger the photothermal responsiveness of the composite hydrogel. Non-photothermal red dye was incorporated in the hydrogels to serve as the on-chip quantitative indicator of the photothermal microfluidic pumping performance. UV–vis absorption spectroscopy characterization of GO and red dye was carried out to confirm their optical absorption properties in the NIR region (Figure S1). In addition, the capillary force-driven traveling behavior of the pure dye solution was studied on a striplike  $\mu\text{PD}$ , demonstrating the feasibility of the red dye as a quantitative indicator of the microfluidic pumping performance (Figure S2).

**NIR Laser-Driven Off-Chip Photothermal Responsiveness of Hydrogels.** To investigate the photothermal responsiveness of the hydrogels to NIR light, the dye-loaded blank and composite hydrogels were irradiated by an 808 nm laser for different times. For comparison, the pure dye solutions and GO-dispersed dye (GO-dye) solutions were irradiated parallelly to the hydrogels. Thermal images of the samples were taken immediately after the irradiation to monitor their temperature changes, as shown in Figure 1E,F. With the increase of the irradiation time from 10 to 110 s, both the GO-doped composite hydrogel and the GO dispersion displayed dramatic temperature increases. A rapid temperature elevation of  $30.8 \text{ }^\circ\text{C}$  was monitored from the composite hydrogel after irradiation for 110 s, while the GO dispersion displayed a 2.3-fold lower elevation value that can be attributed to the higher dilution effect of water to the heat distribution. In contrast, only minor temperature increases of less than  $4.0 \text{ }^\circ\text{C}$  were monitored from the blank NIPAM–AcAm hydrogel and the pure dye solution after irradiation. These results demonstrated strong photothermal effect of GO either doped in the hydrogel or dispersed in the dye solution under laser irradiation.

The NIPAM-derived thermoresponsive hydrogels can undergo structural collapse at temperatures above the LCST with the progressive release of liquids from the hydrogel networks.<sup>22,30</sup> As expected, as the irradiation time increased, the GO-doped composite hydrogel showed gradually increased weight loss, whereas no apparent weight change was observed from the blank NIPAM–AcAm hydrogel (Figure 1G). The result indicated significant phase-transition behavior of the composite hydrogel as a result of the photothermal effect of GO during laser irradiation. It should be noted that rapid weight loss of the GO-doped composite hydrogel started from 50 s with a real-time temperature of  $34.5 \text{ }^\circ\text{C}$ , which might be ascribed to the achievement of the LCST of the hydrogel when rapid phase transition started. The real-time temperature of the composite hydrogel at 50 s was comparable to the LCST (i.e.,  $34.1\text{--}35.5 \text{ }^\circ\text{C}$ ) of GO-doped NIPAM hydrogels as previously

reported in the literature.<sup>22</sup> The off-chip phase transition-based photothermal responsiveness of the composite hydrogel offered the possibility for its further application in on-chip photothermal microfluidic pumping.

**On-Chip Photothermal Microfluidic Pumping under Monitoring of Thermal Imaging.** To demonstrate the possibility of the GO-doped composite hydrogel for photothermal microfluidic pumping, on-chip photothermal responsiveness of the composite hydrogel was investigated on a striplike  $\mu$ PD. For comparison, the hydrogel-loaded  $\mu$ PDs were treated with other approaches including incubation in a water bath at 45 °C and storage at room temperature for 15 min. As shown in Figure 2, both the blank NIPAM–AcAm hydrogel

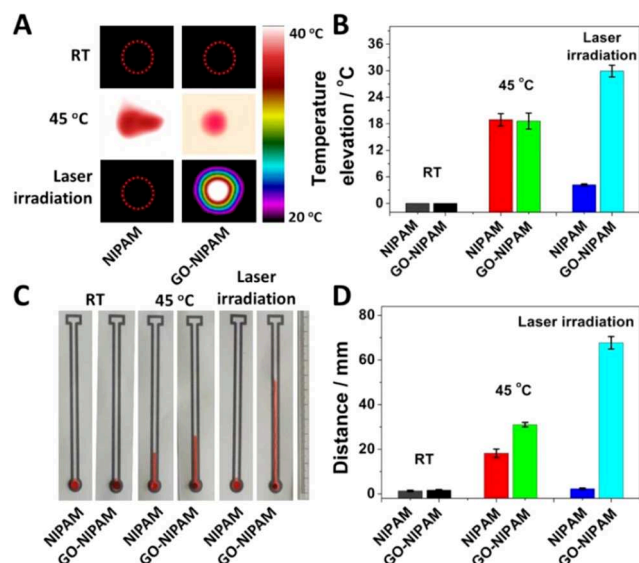


**Figure 2.** On-chip responsiveness of hydrogels to different stimuli. (A) Thermal images of the hydrogels in response to different stimulus on the  $\mu$ PD. (B) Temperature elevations of the hydrogels in response to different stimuli. (C) Photographs of the  $\mu$ PDs in response to different stimuli. (D) On-chip pumping distance of dye solutions from the hydrogels in response to different stimuli. RT, storage of the hydrogels for 10 min at room temperature; 45 °C, incubation of the hydrogels in water bath at 45 °C for 10 min; laser irradiation, irradiation of the hydrogels for 90 s at a power density of 2.2 W·cm<sup>-2</sup>. Error bars indicate standard deviations ( $n = 3$ ).

and the GO-doped composite hydrogel exhibited temperature elevations of around 20 °C after incubation in the water bath, which also displayed on-chip collapse and the simultaneous pumping of dye solutions in the channels. Significantly, the composite hydrogel led to a long dye-traveling distance of 68 mm in channels of the  $\mu$ PD after laser irradiation for only 90 s, illustrating a robust microfluidic pumping behavior because of the aforementioned photothermal responsiveness of the composite hydrogel under laser irradiation. In contrast, the blank NIPAM–AcAm hydrogel showed a minor dye-pumping distance of less than 3.0 mm due to the wicking effect of the paper substrate.<sup>19</sup> It is worth noting that the readout results obtained from the dye-pumping distance were in good agreement with that of the thermal image, suggesting a direct correlation between the photothermal microfluidic pumping performance and the heat generation in the hydrogels. These results demonstrated the successful implementation of the NIR laser-driven photothermal microfluidic pumping strategy on the  $\mu$ PD.

On-chip thermal monitoring is of significant importance to evaluate the performance of heat-involved microfluidic pumping strategies, especially for application in microfluidic pumping of biomolecules. Hence, the on-chip photothermal microfluidic pumping process was monitored by the thermal imaging technique. Figure 3A shows thermal images of the composite hydrogel-loaded  $\mu$ PD at different times before and after laser irradiation. On-chip temperature changes of the composite hydrogel and the dye solution during the microfluidic pumping process can be clearly illustrated in the thermal images. Although the composite hydrogel showed a rapid temperature elevation of 18 °C after irradiation (i.e., at 0 min), the dye solution synchronously pumped in the channel displayed a lower temperature of 20.4 °C that was close to the natural temperature of the  $\mu$ PD. The temperature of the composite hydrogel decreased drastically to 25.7 °C after only 30 s upon removal of the laser irradiation and returned to the initial room temperature rapidly. It was found that there was no apparent temperature elevation in the dye solution in the channel, which might be attributed to the rapid cooling process of the solution as well as the instantly synchronous on-chip pumping process from the hydrogel. These features made the photothermal strategy particularly adaptable for microfluidic pumping of biomolecules.

The photothermal microfluidic pumping performance was investigated as a function of irradiation time, as shown in Figure 3C,D. With the increase of the irradiation time, the on-chip dye-pumping distance of the GO-doped composite hydrogel increased dramatically, whereas the blank NIPAM–AcAm hydrogel exhibited a short dye-pumping distance of less than 3.0 mm at various irradiation times (Figure S3). The saturation of phase transition of the composite hydrogel appeared at the irradiation time of 90 s, followed by minor changes in the dye-pumping distance. These results were consistent with the off-chip weight loss behavior of the hydrogels, as shown in Figure 1G, further indicating the successful implementation of the photothermal microfluidic pumping strategy.

The effect of laser power on the photothermal microfluidic pumping performance was studied on the striplike  $\mu$ PD (Figure 4). As the laser power increased from 0.5 to 2.0 W, the temperature of the composite hydrogel elevated as a result of the progressively enhanced photothermal effect of GO in the hydrogel. Irradiation of the composite hydrogel for only 50 s at a power of 2.0 W led to a considerable temperature increase of 34.1 °C. Corresponding well with the temperature change, the on-chip dye-pumping distance also increased with the elevation of the laser power, which reached a plateau of around 64 mm at 1.4 W due to the achievement of saturated phase transition of the hydrogel.

To study the effect of GO concentration on the photothermal microfluidic pumping performance, the composite hydrogels doped with different concentrations of GO were irradiated for the same time on the  $\mu$ PD. As can be seen in Figure 5, with the increase in concentration of GO from 0.05 to 1.0 mg mL<sup>-1</sup>, both the temperature of the composite hydrogels and the on-chip dye-pumping distance increased gradually, suggesting the dependence of the photothermal microfluidic pumping performance on doping concentration of the photothermal agent in the composite hydrogel. A high temperature elevation of 29.3 °C and a long dye-pumping distance of 59 mm were achieved by the composite hydrogel at a GO concentration of 1.0 mg mL<sup>-1</sup> after laser irradiation for

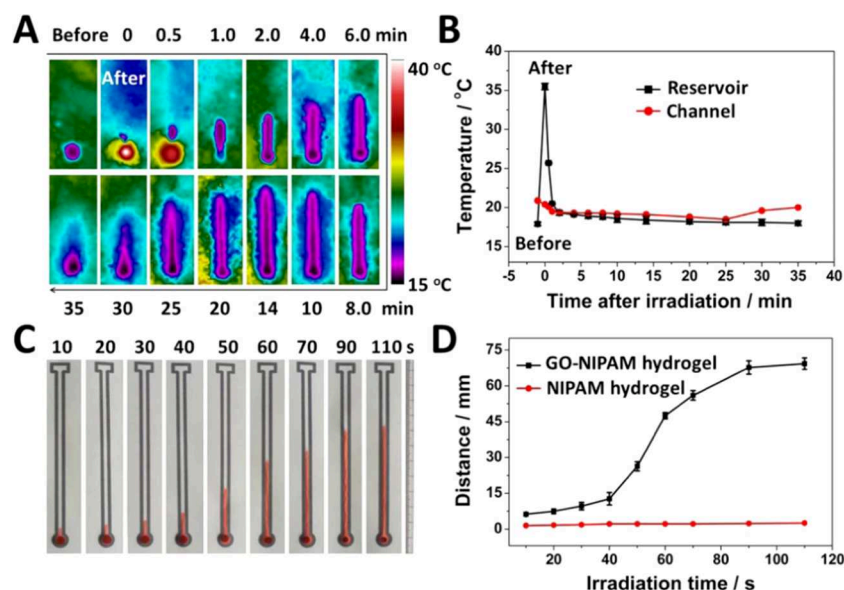


**Figure 3.** On-chip temperature changes during the photothermal microfluidic pumping process and effect of irradiation time on microfluidic pumping performance. (A) Thermal images of the  $\mu$ PD taken at different times before and after laser irradiation of the composite hydrogel for 30 s at a power density of  $2.2 \text{ W}\cdot\text{cm}^{-2}$ . (B) Real-time temperatures of the composite hydrogel and the dye solution in the channel before and after the irradiation. (C) Photographs of the  $\mu$ PDs after laser irradiation of the composite hydrogels for different times. (D) On-chip pumping distance of dye solutions from the hydrogels after the irradiation. Error bars indicate standard deviations ( $n = 3$ ).

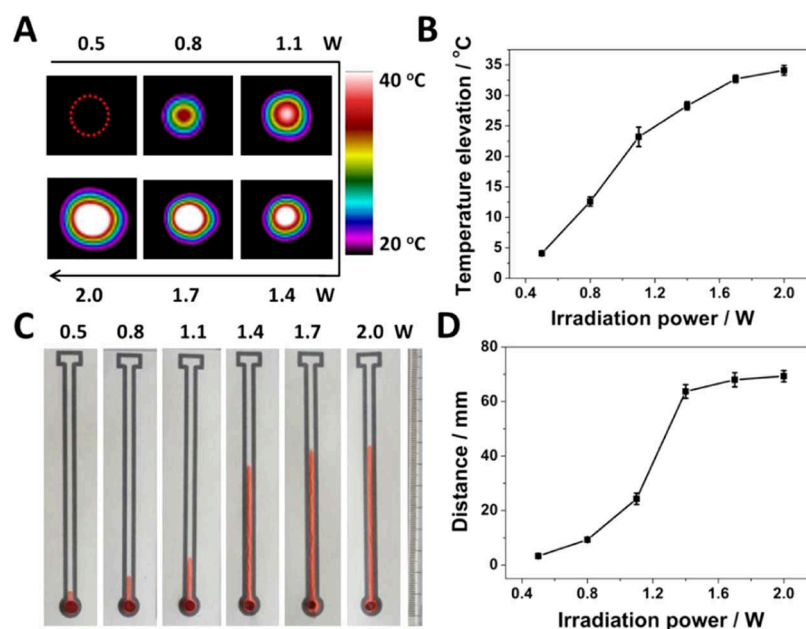


**Figure 4.** Effect of laser power on photothermal microfluidic pumping performance. (A) On-chip thermal images of the composite hydrogels after the laser irradiation for 50 s at different laser powers. (B) Temperature elevation of the hydrogels as a function of laser power. (C) Photographs of the  $\mu$ PDs after the irradiation. (D) On-chip pumping distance of dye solutions from the hydrogels after the irradiation. Error bars indicate standard deviations ( $n = 3$ ).

only 50 s. Both the temperature elevation value and the dye-pumping distance were proportional to the GO concentration in the range from  $0.1$  to  $1.0 \text{ mg mL}^{-1}$  with correlation coefficients of  $0.993$  and  $0.995$ , respectively. Similar linear relationships between the concentrations of photothermal agents and the photothermal effect-induced temperature elevation values had been reported in our previous works.<sup>48,49</sup> Therefore, by remotely adjusting the parameter settings of the laser pointer and altering the doping concentration of GO in the composite hydrogel, the on-chip

photothermal microfluidic pumping performance can be precisely controlled in a quantitative way.

To assess the precision and reproducibility of the microfluidic pumping strategy, the composite hydrogels prepared from both the same and different batches were irradiated parallelly on the  $\mu$ PD. After irradiation of six pieces of the hydrogels on the  $\mu$ PD, on-chip measurements of both the temperature change and the dye-pumping distance resulted in relative standard deviations of lower than  $7.0\%$  (Figures S4 and S5), indicating high precision and reproducibility of the

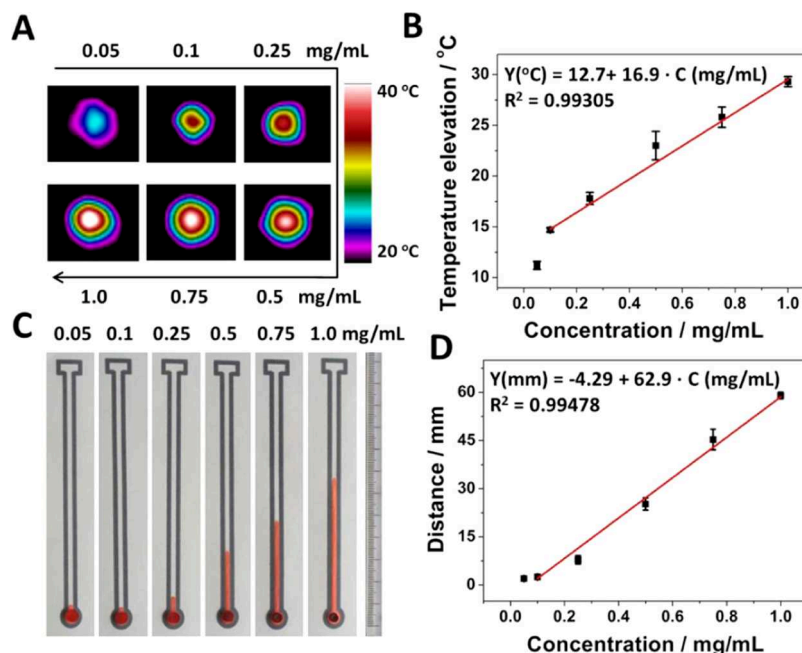


**Figure 5.** Effect of GO concentration on the photothermal microfluidic pumping performance. (A) Thermal images of the composite hydrogels doped with different concentrations of GO after the laser irradiation for 50 s at a power density of  $2.2 \text{ W}\cdot\text{cm}^{-2}$ . (B) Calibration plot of temperature elevation value of the hydrogels vs GO concentration. (C) Photographs of the  $\mu$ PDs after the irradiation. (D) Calibration plot of on-chip pumping distance of dye solutions from the hydrogels vs GO concentration. Error bars indicate standard deviations ( $n = 3$ ).

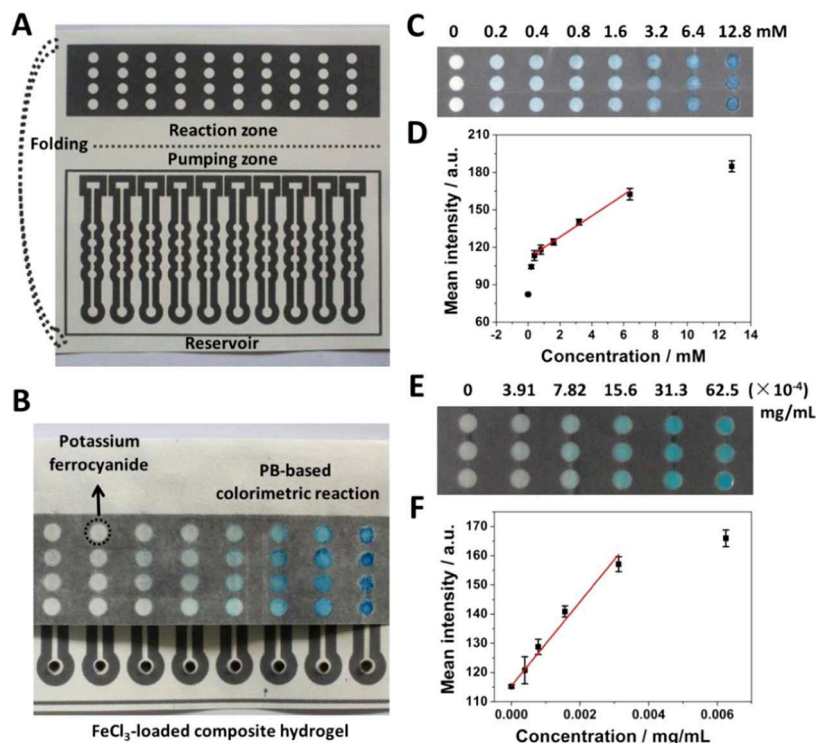


**Figure 6.** On-chip photothermal microfluidic pumping of  $\text{FeCl}_3$  and HRP. (A) Design and photograph of the 3D foldable  $\mu$ PD. (B) Photographic illustration of working principle of the on-chip PB-based colorimetric reaction. (C) Photograph of the reaction zone obtained from on-chip photothermal pumping of different concentrations of  $\text{FeCl}_3$  from the composite hydrogels. (D) Color intensity of the reaction wells as a function of  $\text{FeCl}_3$  concentration. (E) Photograph of the reaction zone obtained from on-chip photothermal pumping of different concentrations of HRP from the composite hydrogels. (F) Color intensity of the reaction wells as a function of HRP concentration. The composite hydrogels of 4.0 mm thickness were irradiation for 130 s at a power density of  $2.2 \text{ W}\cdot\text{cm}^{-2}$  on the  $\mu$ PD. Error bars indicate standard deviations ( $n = 3$ ).

microfluidic pumping strategy. Furthermore, excellent recovery of the microfluidic pumping efficiency was demonstrated upon multiple cycles of reusage of the composite hydrogel on the

$\mu$ PD (Figure S6), owing to the intrinsic reversible phase-transition property of the NIPAM-derived thermoresponsive hydrogels in response to thermal stimulus.<sup>22,30</sup>

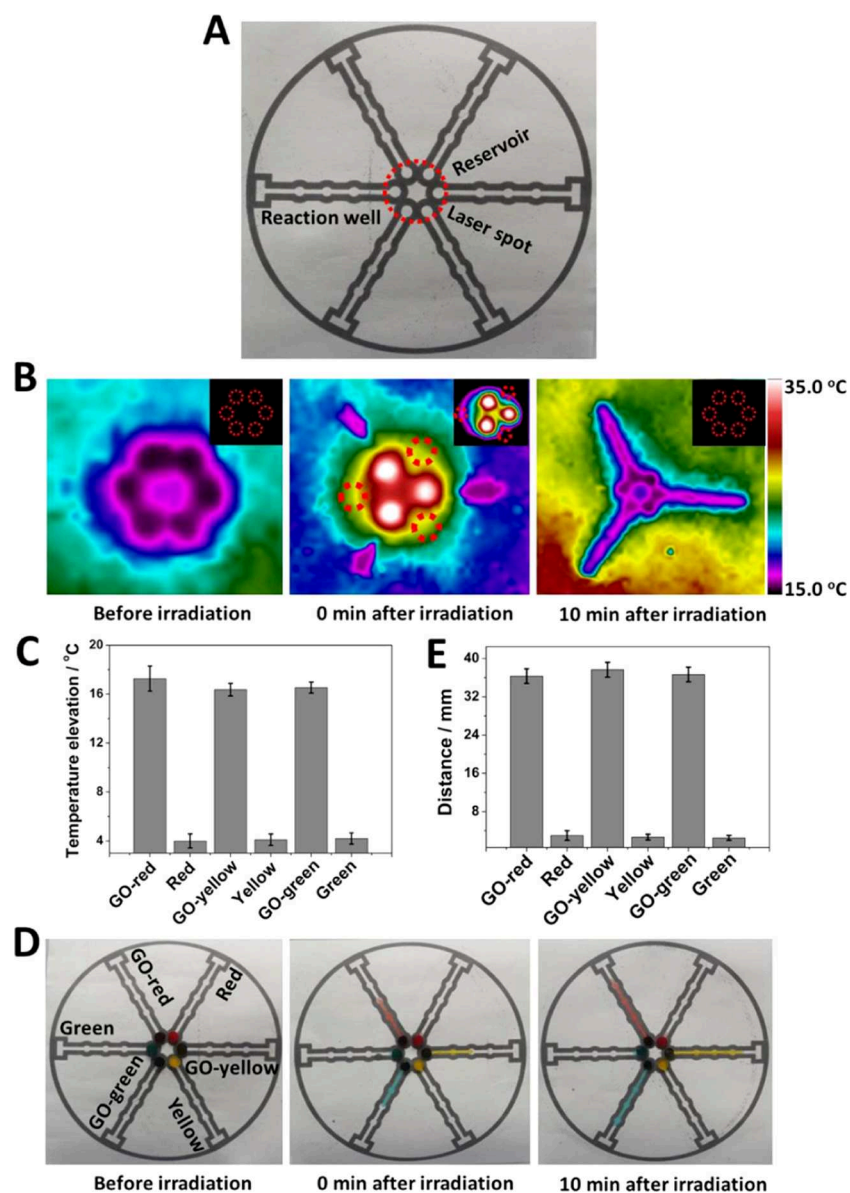


**Figure 7.** On-chip multiplexed photothermal microfluidic pumping. (A) Design and photograph of the disklike  $\mu$ PD. (B) Thermal images of the  $\mu$ PD with (i.e., GO-red, GO-yellow, and GO-green) and without (i.e., red, yellow, and green) doping of GO in the hydrogels before and after laser irradiation for 150 s at a power density of  $0.38 \text{ W}\cdot\text{cm}^{-2}$ . Inset: Thermal images with a temperature scale from 20 to 35 °C. (C) Temperature elevations of the hydrogels after irradiation. (D) Photographs of the  $\mu$ PD before and after irradiation. (E) On-chip pumping distance of dye solutions from the hydrogels after irradiation. Error bars indicate standard deviations ( $n = 3$ ).

**Exemplification of the Photothermal Microfluidic Pumping Strategy.** To exemplify the photothermal pumping strategy for practical microfluidic applications, a 3D foldable  $\mu$ PD was designed to implement the on-chip PB-based colorimetric reaction using  $\text{FeCl}_3$  as the model transport cargo. The  $\mu$ PD was composed of a pumping zone and a reaction zone, as shown in Figure 6. Different concentrations of  $\text{FeCl}_3$  solutions were loaded in the composite hydrogels that served as the photothermally responsive cargo reservoirs on the pumping zone. Potassium ferrocyanide as the reaction substrate was deposited in the reaction wells. The reaction zone was folded toward the pumping zone to enable the compact contact between the reaction wells and the pumping channels. Upon laser irradiation of the composite hydrogels for only 130 s, a rapid and homogeneous microfluidic pumping of  $\text{FeCl}_3$  solutions from the reservoirs to arrays of reaction wells

was successively achieved, leading to uniform colorimetric displays in the reaction wells as a result of the on-chip production of PB. The color intensity of the reaction wells was linearly associated with the concentration of  $\text{FeCl}_3$  in the range from 0.4 to 6.4 mM with a correlation coefficient of 0.985. The result suggested excellent linear correlation between the original  $\text{FeCl}_3$  concentration in the hydrogel and the final concentration pumped to the reaction wells.

To further exemplify the new strategy for practical microfluidic pumping of biomolecules, HRP was chosen as the model transport biomolecule to perform the typical on-chip TMB-based colorimetric reaction. TMB- $\text{H}_2\text{O}_2$  solutions were deposited in the reaction wells to act as the substrate of the HRP-catalyzed colorimetric reaction.<sup>49</sup> Similarly, HRP solutions in the composite hydrogels were also successfully pumped to arrays of reaction wells with the appearance of

uniform color changes, the intensity of which was proportional to the HRP concentration in the range from 0 to  $3.13 \times 10^{-3}$  mg mL<sup>-1</sup> with a correlation coefficient of 0.986. The result indicated that the enzymatic activity of HRP was well remained during the on-chip photothermal microfluidic pumping process, which can be attributed to the modest thermal variation of solutions during the pumping process as discussed in Figure 3A,B. However, in comparison with the above colorimetric results, the same concentrations of the pure HRP solutions resulted in relatively higher color intensities on the  $\mu$ PD (Figure S7). It was believed that the physical attachment of a minor amount of HRP in the GO-doped hydrogel networks was inevitable, which might lead to incomplete release of HRP during the on-chip photothermal pumping process.

**Multiplexed On-Demand Photothermal Microfluidic Pumping.** To realize on-chip photothermal microfluidic pumping in a multiplexed manner, a new disklike  $\mu$ PD was designed with the compact integration of multiple reservoirs in the device center, as shown in Figure 7A. By simply adjusting the spatial distance between the  $\mu$ PD and the laser pointer, the laser spot can be tuned to cover either all of the reservoirs or some of the predefined regions. In this way, simultaneous on-demand microfluidic pumping from multiple hydrogels can be realized upon a single laser irradiation process. As expected, upon a single irradiation process for only 150 s, three pieces of the composite hydrogels doped with the same concentration of GO exhibited uniform temperature elevations with the vivid thermal display of the microfluidic pumping process in a multiplexed manner (Figure 7B). Accordingly, different dye solutions were uniformly pumped from the central reservoirs to arrays of reaction wells, whereas the blank hydrogels exhibited both no apparent temperature elevation and no dye release. It should be noted that the reservoir quantity and the microfluidic pumping pathway can be flexibly adjusted by tuning the irradiation distance and the microfluidic pattern. In addition, by spatiotemporally controlling the parameter settings of the laser pointer and altering the doping concentration of GO in the hydrogel, multiplexed on-demand microfluidic pumping with varying outputs can be achieved in a quantitative way.

## CONCLUSIONS

In combination with GO-doped photothermally responsive hydrogels, the NIR laser-driven photothermal effect has been exploited in  $\mu$ PDs to develop a photothermal microfluidic pumping strategy. On-chip phase transition of the composite hydrogels can be actuated in a switchlike manner in response to remote NIR laser irradiation, enabling highly robust microfluidic pumping of cargoes from the hydrogels in a contactless and spatiotemporally controllable fashion. We have exemplified the practical microfluidic application of the new strategy by FeCl<sub>3</sub> and HRP as the model transport cargoes. More importantly, multiplexed on-demand microfluidic pumping was achieved by flexibly adjusting the irradiation pathway and the microfluidic pattern. The photothermal microfluidic pumping strategy holds broad applicability at most common experimental temperatures below the LCST (i.e., 34–35 °C) of the composite hydrogels, owing to the intrinsic phase-transition property of the photothermally responsive hydrogels. In comparison with the previously reported microfluidic pumping method using inseparable heating plates as the heat sources,<sup>17,19</sup> the new strategy is particularly

advantageous because of the ease of an NIR laser pointer for lab-on-a-chip operations, such as high integratability into lab-on-a-chip devices, switchlike instant controllability, and remote targeting capability. Furthermore, the photothermal agent composited in the thermoresponsive hydrogel is not confined to GO, but can be extended to a wide range of photothermal materials. Therefore, the new photothermal microfluidic pumping strategy shows great potential to implement diverse microfluidic liquid- and cargo-handling protocols, due to its flexibility, high integratability into lab-on-a-chip devices, and contactless and spatiotemporal controllability.

## ASSOCIATED CONTENT

### Supporting Information

The Supporting Information is available free of charge on the ACS Publications website at DOI: 10.1021/acssensors.9b01109.

Hydrogel synthesis; UV–vis absorption spectroscopic characterization; effect of irradiation time; precision and reproducibility; recovery of photothermal microfluidic pumping efficiency (PDF)

## AUTHOR INFORMATION

### Corresponding Authors

\*E-mail: fuguanglei@nbu.edu.cn (G.F.).

\*E-mail: xli4@utep.edu (X.L.).

### ORCID

Guanglei Fu: 0000-0002-8128-1224

XiuJun Li: 0000-0002-7954-0717

### Notes

The authors declare no competing financial interest.

## ACKNOWLEDGMENTS

This work was financially supported by the National Natural Science Foundation of China (No. 81701790). The authors are also grateful to the financial support from the Research Starting Foundation of Ningbo University (No. 014-421804870), the U.S. NSF-PREM program (No. DMR 1827745), and the National Natural Science Foundation of China (No. 81700436).

## REFERENCES

- (1) Martinez, A. W.; Phillips, S. T.; Butte, M. J.; Whitesides, G. M. Patterned paper as a platform for inexpensive, low-volume, portable bioassays. *Angew. Chem., Int. Ed.* **2007**, *46*, 1318–1320.
- (2) Sun, J.; Xianyu, Y.; Jiang, X. Point-of-care biochemical assays using gold nanoparticle-implemented microfluidics. *Chem. Soc. Rev.* **2014**, *43*, 6239–6253.
- (3) Cate, D. M.; Adkins, J. A.; Mettakoonpitak, J.; Henry, C. S. Recent developments in paper-based microfluidic devices. *Anal. Chem.* **2015**, *87*, 19–41.
- (4) Sanjay, S. T.; Zhou, W.; Dou, M.; Tavakoli, H.; Ma, L.; Xu, F.; Li, X. Recent advances of controlled drug delivery using microfluidic platforms. *Adv. Drug Delivery Rev.* **2018**, *128*, 3–28.
- (5) Sanjay, S. T.; Fu, G.; Dou, M.; Xu, F.; Liu, R.; Qi, H.; Li, X. Biomarker detection for disease diagnosis using cost-effective microfluidic platforms. *Analyst* **2015**, *140*, 7062–7081.
- (6) Nyein, H. Y. Y.; Tai, L.; Ngo, Q. P.; Chao, M.; Zhang, G.; Gao, W.; Bariya, M.; Bullock, J.; Kim, H.; Fahad, H. M. A Wearable Microfluidic Sensing Patch for Dynamic Sweat Secretion Analysis. *ACS Sens.* **2018**, *3*, 944–952.
- (7) Tian, T.; Wei, X.; Jia, S.; Zhang, R.; Li, J.; Zhu, Z.; Zhang, H.; Ma, Y.; Lin, Z.; Yang, C. J. Integration of target responsive hydrogel

with cascaded enzymatic reactions and microfluidic paper-based analytic devices ( $\mu$ PADs) for point-of-care testing (POCT). *Biosens. Bioelectron.* **2016**, *77*, 537–542.

(8) Lim, W. Y.; Thevarajah, T. M.; Goh, B. T.; Khor, S. M. Paper microfluidic device for early diagnosis and prognosis of acute myocardial infarction via quantitative multiplex cardiac biomarker detection. *Biosens. Bioelectron.* **2019**, *128*, 176–185.

(9) Sun, X.; Wang, H.; Jian, Y.; Lan, F.; Zhang, L.; Liu, H.; Ge, S.; Yu, J. Ultrasensitive microfluidic paper-based electrochemical/visual biosensor based on spherical-like cerium dioxide catalyst for miR-21 detection. *Biosens. Bioelectron.* **2018**, *105*, 218–225.

(10) He, M.; Liu, Z. Paper-based microfluidic device with upconversion fluorescence assay. *Anal. Chem.* **2013**, *85*, 11691–11694.

(11) Wang, Y.; Luo, J.; Liu, J.; Li, X.; Kong, Z.; Jin, H.; Cai, X. Electrochemical integrated paper-based immunosensor modified with multi-walled carbon nanotubes nanocomposites for point-of-care testing of  $17\beta$ -estradiol. *Biosens. Bioelectron.* **2018**, *107*, 47–53.

(12) Wang, C.; Hennek, J. W.; Ainla, A.; Kumar, A.; Lan, W.; Im, J. S.; Smith, B. S.; Zhao, M.; Whitesides, G. M. A Paper-Based “Pop-up” Electrochemical Device for Analysis of Beta-Hydroxybutyrate. *Anal. Chem.* **2016**, *88*, 6326–6333.

(13) Martín, A.; Kim, J.; Kurniawan, J. F.; Sempionatto, J. R.; Moreto, J. R.; Tang, G.; Campbell, A. S.; Shin, A.; Lee, M. Y.; Liu, X.; Wang, J. Epidermal Microfluidic Electrochemical Detection System: Enhanced Sweat Sampling and Metabolite Detection. *ACS Sens.* **2017**, *2*, 1860–1868.

(14) Yakoh, A.; Chaiyo, S.; Siangproh, W.; Chailapakul, O. 3D Capillary-Driven Paper-Based Sequential Microfluidic Device for Electrochemical Sensing Applications. *ACS Sens.* **2019**, *4*, 1211–1221.

(15) Wei, X.; Zhou, W.; Sanjay, S. T.; Zhang, J.; Jin, Q.; Xu, F.; Dominguez, D. C.; Li, X. Multiplexed Instrument-Free Bar-Chart SpinChip Integrated with Nanoparticle-Mediated Magnetic Aptasensors for Visual Quantitative Detection of Multiple Pathogens. *Anal. Chem.* **2018**, *90*, 9888–9896.

(16) Dou, M.; Macias, N.; Shen, F.; Bard, J. D.; Dominguez, D. C.; Li, X. Rapid and Accurate Diagnosis of the Respiratory Disease Pertussis on a Point-of-Care Biochip. *EClinicalMedicine* **2019**, *8*, 72–77.

(17) Niedl, R. R.; Beta, C. Hydrogel-driven paper-based microfluidics. *Lab Chip* **2015**, *15*, 2452–2459.

(18) Channon, R. B.; Nguyen, M. P.; Scorzelli, A. G.; Henry, E. M.; Volckens, J.; Dandy, D. S.; Henry, C. S. Rapid flow in multilayer microfluidic paper-based analytical devices. *Lab Chip* **2018**, *18*, 793–802.

(19) Mitchell, H. T.; Schultz, S. A.; Costanzo, P. J.; Martinez, A. W. Poly(N-isopropylacrylamide) Hydrogels for Storage and Delivery of Reagents to Paper-Based Analytical Devices. *Chromatography* **2015**, *2*, 436–451.

(20) Fu, X.; Mavrogiannis, N.; Doria, S.; Gagnon, Z. Microfluidic pumping, routing and metering by contactless metal-based electroosmosis. *Lab Chip* **2015**, *15*, 3600–3608.

(21) Chou, P. Y.; Chen, S. H.; Chen, C. H.; Chen, S. H.; Teng, F. Y.; Chen, J. P. Thermo-responsive in-situ forming hydrogels as barriers to prevent post-operative peritendinous adhesion. *Acta Biomater.* **2017**, *63*, 85–95.

(22) Zhu, C.; Lu, Y.; Peng, J.; Chen, J.; Yu, S. Photothermally Sensitive Poly(N-isopropylacrylamide)/Graphene Oxide Nanocomposite Hydrogels as Remote Light-Controlled Liquid Microvalves. *Adv. Funct. Mater.* **2012**, *22*, 4017–4022.

(23) Lv, S.-W.; Liu, Y.; Xie, M.; Wang, J.; Yan, X.-W.; Li, Z.; Dong, W.-G.; Huang, W.-H. Near-Infrared Light-Responsive Hydrogel for Specific Recognition and Photothermal Site-Release of Circulating Tumor Cells. *ACS Nano* **2016**, *10*, 6201–6210.

(24) Wu, C.; Sun, M.; Shieh, J.; Chen, C.; Huang, C.; Dai, C.; Chang, S.; Chen, W.; Young, T. Ultrasound-responsive NIPAM-based hydrogels with tunable profile of controlled release of large molecules. *Ultrasonics* **2018**, *83*, 157–163.

(25) Zhao, L.; Yin, S.; Ma, Z.  $\text{Ca}^{2+}$ -Triggered pH-Response Sodium Alginate Hydrogel Precipitation for Amplified Sandwich-Type Impedimetric Immunosensor of Tumor Marker. *ACS Sens.* **2019**, *4*, 450–455.

(26) Qu, Y.; Chu, B. Y.; Peng, J. R.; Liao, J. F.; Qi, T. T.; Shi, K.; Zhang, X. N.; Wei, Y. Q.; Qian, Z. Y. A biodegradable thermo-responsive hybrid hydrogel: therapeutic applications in preventing the post-operative recurrence of breast cancer. *NPG Asia Mater.* **2015**, *7*, No. e207.

(27) Wang, X.; Wang, C.; Wang, X.; Wang, Y.; Zhang, Q.; Cheng, Y. A Polydopamine Nanoparticle-Knotted Poly(ethylene glycol) Hydrogel for On-Demand Drug Delivery and Chemo-photothermal Therapy. *Chem. Mater.* **2017**, *29*, 1370–1376.

(28) Hosoya, H.; Dobroff, A. S.; Driessen, W. H. P.; Cristini, V.; Brinker, L. M.; Staquicini, F. I.; Cardovila, M.; Dangelo, S.; Ferrara, F.; Prometh, B.; Lin, Y.-S.; Dunphy, D. R.; Dogra, P.; Melancon, M. P.; Stafford, R. J.; Miyazono, K.; Gelovani, J. G.; Kataoka, K.; Brinker, C. J.; Sidman, R. L.; Arap, W.; Pasqualini, R. Integrated nanotechnology platform for tumor-targeted multimodal imaging and therapeutic cargo release. *Proc. Natl. Acad. Sci. U.S.A.* **2016**, *113*, 1877–1882.

(29) Fathi, M.; Alami-Milani, M.; Geranmayeh, M. H.; Barar, J.; Erfan-Niya, H.; Omid, Y. Dual thermo- and pH-sensitive injectable hydrogels of chitosan/(poly(N-isopropylacrylamide-co-itaconic acid)) for doxorubicin delivery in breast cancer. *Int. J. Biol. Macromol.* **2019**, *128*, 957–964.

(30) Zhu, C.; Lu, Y.; Chen, J.; Yu, S. Photothermal Poly(N-isopropylacrylamide)/ $\text{Fe}_3\text{O}_4$  Nanocomposite Hydrogel as a Movable Position Heating Source under Remote Control. *Small* **2014**, *10*, 2796–2800.

(31) Chen, S.; Tang, F.; Tang, L.; Li, L. Synthesis of Cu-Nanoparticle Hydrogel with Self-Healing and Photothermal Properties. *ACS Appl. Mater. Interfaces* **2017**, *9*, 20895–20903.

(32) Zhang, E.; Guo, Q.; Ji, F.; Tian, X.; Cui, J.; Song, Y.; Sun, H.; Li, J.; Yao, F. Thermoresponsive polysaccharide-based composite hydrogel with antibacterial and healing-promoting activities for preventing recurrent adhesion after adhesiolysis. *Acta Biomater.* **2018**, *74*, 439–453.

(33) Ghavaminejad, A.; Samarikhajaj, M.; Aguilar, L. E.; Park, C. H.; Kim, C. S. pH/NIR Light-Controlled Multidrug Release via a Mussel-Inspired Nanocomposite Hydrogel for Chemo-Photothermal Cancer Therapy. *Sci. Rep.* **2016**, *6*, No. 33594.

(34) Shen, X.; Yang, X.; Su, C.; Yang, J.; Zhang, L.; Liu, B.; Gao, S.; Gai, F.; Shao, Z.; Gao, G. Thermo-responsive photoluminescent silver clusters/hydrogel nanocomposites for highly sensitive and selective detection of Cr(VI). *J. Mater. Chem. C* **2018**, *6*, 2088–2094.

(35) Fu, G.; Liu, W.; Li, Y.; Jin, Y.; Jiang, L.; Liang, X.; Feng, S.; Dai, Z. Magnetic Prussian blue nanoparticles for targeted photothermal therapy under magnetic resonance imaging guidance. *Bioconjugate Chem.* **2014**, *25*, 1655–1663.

(36) Lu, G. H.; Shang, W. T.; Deng, H.; Han, Z. Y.; Hu, M.; Liang, X. Y.; Fang, C. H.; Zhu, X. H.; Fan, Y. F.; Tian, J. Targeting carbon nanotubes based on IGF-1R for photothermal therapy of orthotopic pancreatic cancer guided by optical imaging. *Biomaterials* **2019**, *195*, 13–22.

(37) Bao, Y. W.; Hua, X. W.; Li, Y. H.; Jia, H. R.; Wu, F. G. Hyperthermia-Promoted Cytosolic and Nuclear Delivery of Copper/Carbon Quantum Dot-Crosslinked Nanosheets: Multimodal Imaging-Guided Photothermal Cancer Therapy. *ACS Appl. Mater. Interfaces* **2018**, *10*, 1544–1555.

(38) Fu, G.; Liu, W.; Feng, S.; Yue, X. Prussian blue nanoparticles operate as a new generation of photothermal ablation agents for cancer therapy. *Chem. Commun.* **2012**, *48*, 11567–11569.

(39) Bertorelle, F.; Pinto, M.; Zappone, R.; Pilot, R.; Litti, L.; Fiameni, S.; Conti, G.; Gobbo, M.; Toffoli, G.; Colombatti, M.; Fracasso, G.; Meneghetti, M. Safe core-satellite magneto-plasmonic nanostructures for efficient targeting and photothermal treatment of tumor cells. *Nanoscale* **2018**, *10*, 976–984.

(40) Cai, K.; Zhang, W.; Zhang, J.; Li, H.; Han, H.; Zhai, T. Design of Gold Hollow Nanorods with Controllable Aspect Ratio for

Multimodal Imaging and Combined Chemo-Photothermal Therapy in the Second Near-Infrared Window. *ACS Appl. Mater. Interfaces* **2018**, *10*, 36703–36710.

(41) Dong, L.; Ji, G.; Liu, Y.; Xu, X.; Lei, P.; Du, K.; Song, S.; Feng, J.; Zhang, H. Multifunctional Cu-Ag<sub>2</sub>S nanoparticles with high photothermal conversion efficiency for photoacoustic imaging-guided photothermal therapy in vivo. *Nanoscale* **2018**, *10*, 825–831.

(42) Wan, H.; Zhang, Y.; Liu, Z.; Xu, G.; Huang, G.; Ji, Y.; Xiong, Z.; Zhang, Q.; Dong, J.; Zhang, W.; Zou, H. Facile fabrication of a near-infrared responsive nanocarrier for spatiotemporally controlled chemo-photothermal synergistic cancer therapy. *Nanoscale* **2014**, *6*, 8743–8753.

(43) Nam, J.; La, W.-G.; Hwang, S.; Ha, Y. S.; Park, N.; Won, N.; Jung, S.; Bhang, S. H.; Ma, Y.-J.; Cho, Y.-M.; Jin, M.; Han, J.; Shin, J.-Y.; Wang, E. K.; Kim, S. G.; Cho, S.-H.; Yoo, J.; Kim, B.-S.; Kim, S. pH-responsive assembly of gold nanoparticles and “spatiotemporally concerted” drug release for synergistic cancer therapy. *ACS Nano* **2013**, *7*, 3388–3402.

(44) Jadhav, A. D.; Yan, B.; Luo, R. C.; Wei, L.; Zhen, X.; Chen, C. H.; Shi, P. Photoresponsive microvalve for remote actuation and flow control in microfluidic devices. *Biomicrofluidics* **2015**, *9*, No. 034114.

(45) Lim, J. H.; Kim, D. E.; Kim, E.; Ahrberg, C. D.; Chung, B. G. Functional Graphene Oxide-Based Nanosheets for Photothermal Therapy. *Macromol. Res.* **2018**, *26*, 557–565.

(46) Zhang, W.; Guo, Z.; Huang, D.; Liu, Z.; Guo, X.; Zhong, H. Synergistic effect of chemo-photothermal therapy using PEGylated graphene oxide. *Biomaterials* **2011**, *32*, 8555–8561.

(47) Ma, X.; Tao, H.; Yang, K.; Feng, L.; Cheng, L.; Shi, X.; Li, Y.; Guo, L.; Liu, Z. A functionalized graphene oxide-iron oxide nanocomposite for magnetically targeted drug delivery, photothermal therapy, and magnetic resonance imaging. *Nano Res.* **2012**, *5*, 199–212.

(48) Fu, G.; Sanjay, S. T.; Dou, M.; Li, X. Nanoparticle-mediated photothermal effect enables a new method for quantitative biochemical analysis using a thermometer. *Nanoscale* **2016**, *8*, 5422–5427.

(49) Fu, G.; Sanjay, S. T.; Zhou, W.; Brekken, R. A.; Kirken, R. A.; Li, X. Exploration of Nanoparticle-Mediated Photothermal Effect of TMB-H<sub>2</sub>O<sub>2</sub> Colorimetric System and Its Application in a Visual Quantitative Photothermal Immunoassay. *Anal. Chem.* **2018**, *90*, 5930–5937.